IEEE Transactions on Geoscience and Remote Sensing

Supplementary Materials for

Towards Long-Wavelength Ionospheric Correction of InSAR Time Series Using GNSS-Based TEC

Yidi Wang[1,2], Zhang Yunjun[1,2*], Ningbo Wang[2,3], Runqing Liu[2,3],
Cunren Liang[4], Yosuke Aoki[5], and Robert Wang[1,2]

[1]National Key Laboratory of Microwave Imaging, Aerospace Information Research Institute, Chinese Academy of Sciences, Beijing, China
[2]School of Electronics, Electrical and Communication Engineering, University of Chinese Academy of Sciences, Beijing, China
[3]Aerospace Information Research Institute, Chinese Academy of Sciences, Beijing, China
[4]Institute of Remote Sensing and Geographic Information System, School of Earth and Space Sciences, Peking University, Beijing, China
[5]Earthquake Research Institute, University of Tokyo, Tokyo, Japan
*Corresponding author: Zhang Yunjun

Content of this file

S1. Supplemental figures

This section provides Figures S1 to S10. Fig. S1 shows the interferogram networks of all interferograms used in this study. Fig. S2 shows the average value of the spatial coherence of all interferograms used in this study. Fig. S3 shows the temporal coherence of all interferograms used in this study. Figs. S4-S10 show the different phase time series for Sentinel-1 ascending track 166 in western USA.

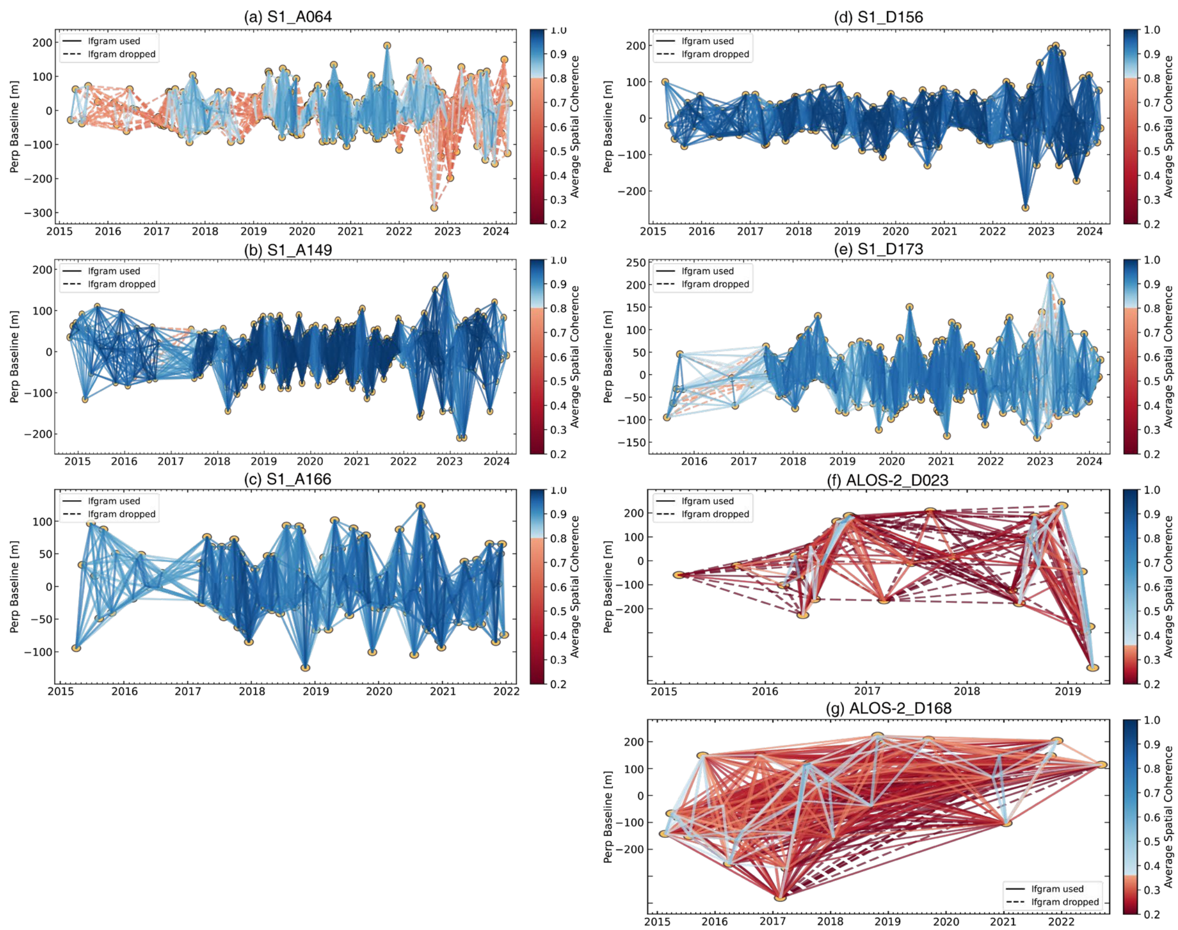

Figure S1. The interferogram network of all Sentinel-1 and ALOS-2 tracks. Solid lines represent the interferograms used for subsequent network inversion to estimate the time series, while dashed lines represent the interferograms discarded due to low spatial coherence.

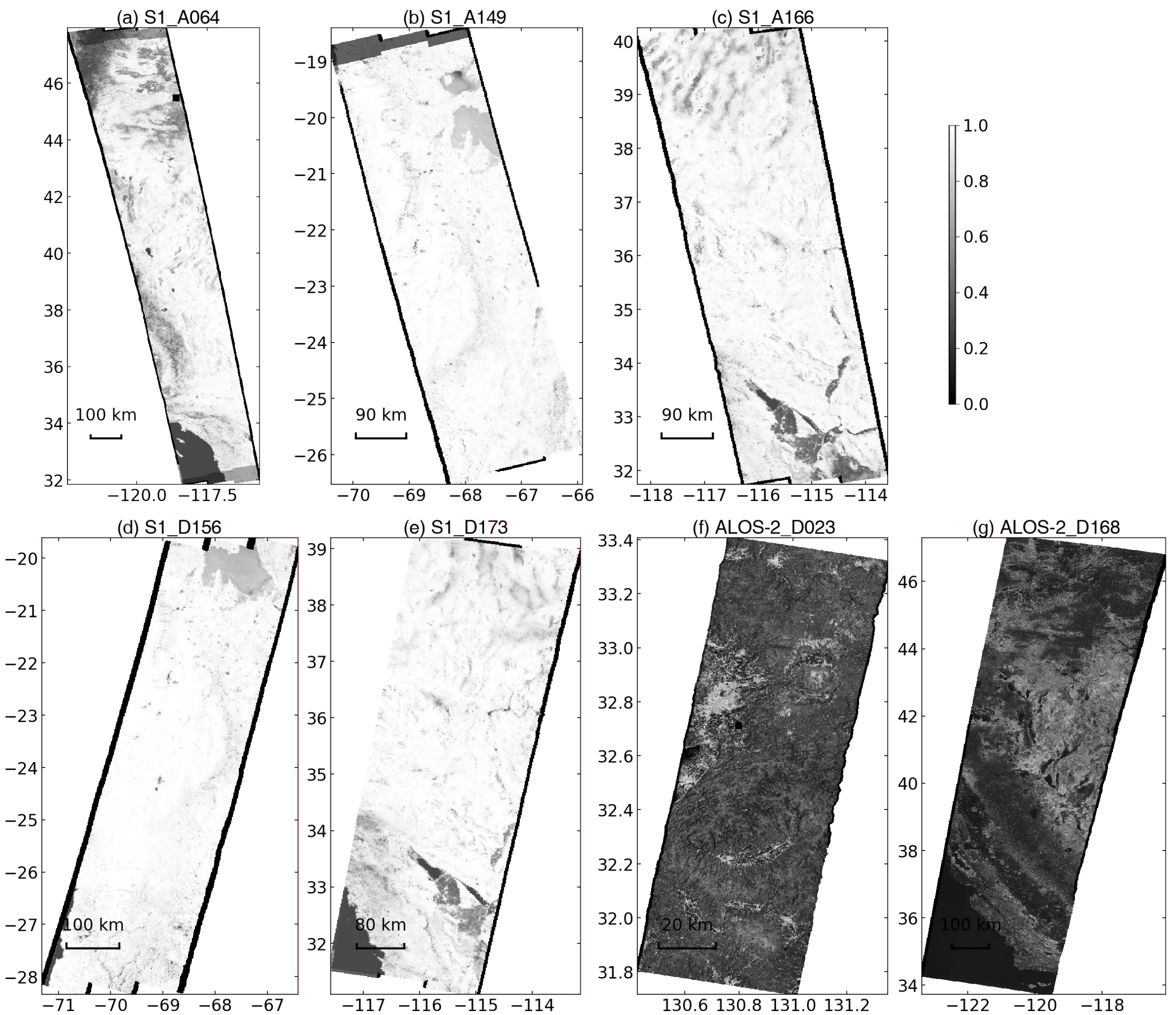

Figure S2. The average spatial coherence of all Sentinel-1 and ALOS-2 tracks. The spatial coherence of the C-band Sentinel-1 (a)-(e) is calculated from the phase standard deviation using equation (12) in Agram & Simons (2015) [1], while the spatial coherence of the L-band ALOS-2 (f)-(g) is calculated using the complex coherence from SLCs using equation (11) in Agram & Simons (2015) [1].

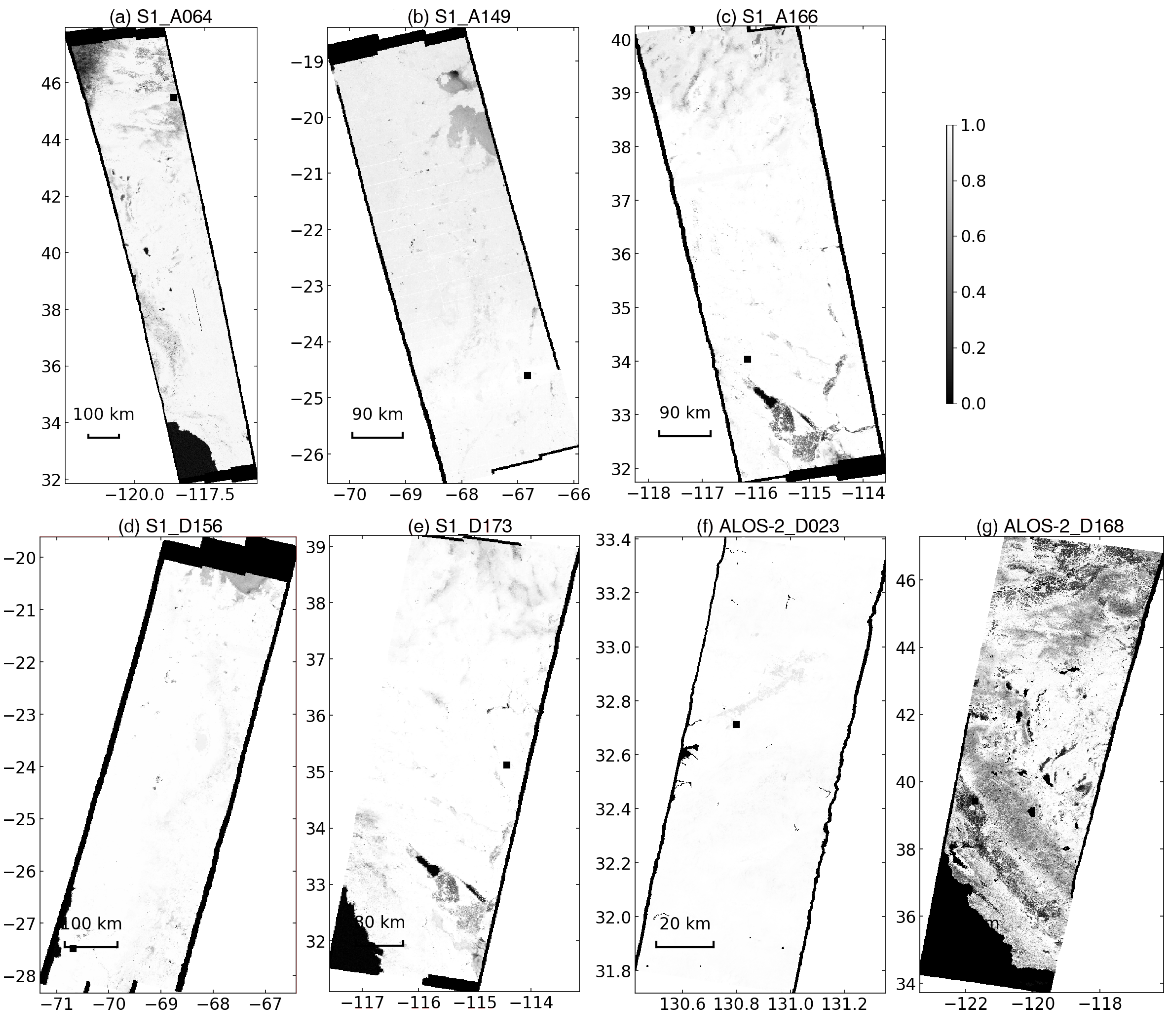

Figure S3. The temporal coherence of all Sentinel-1 and ALOS-2 tracks. The temporal coherence is calculated using equation (16) in Pepe et al. (2006) [2].

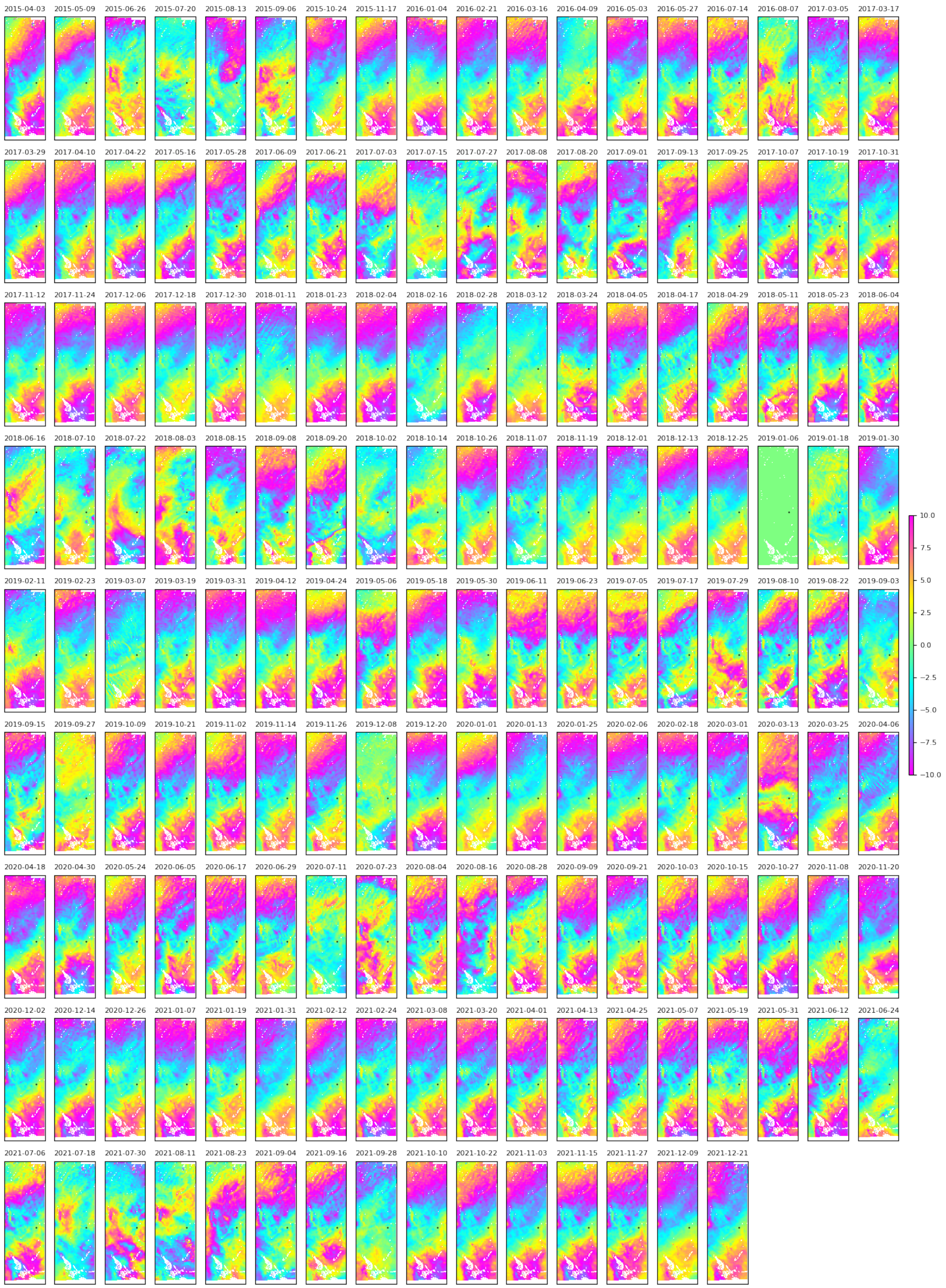

Figure S4. The raw phase time series of Sentinel-1 ascending track 166 in western USA. The data is rewrapped into [-10, 10) cm for display. Black square donates the spatial reference point at 35.8°N, 114.9°W.

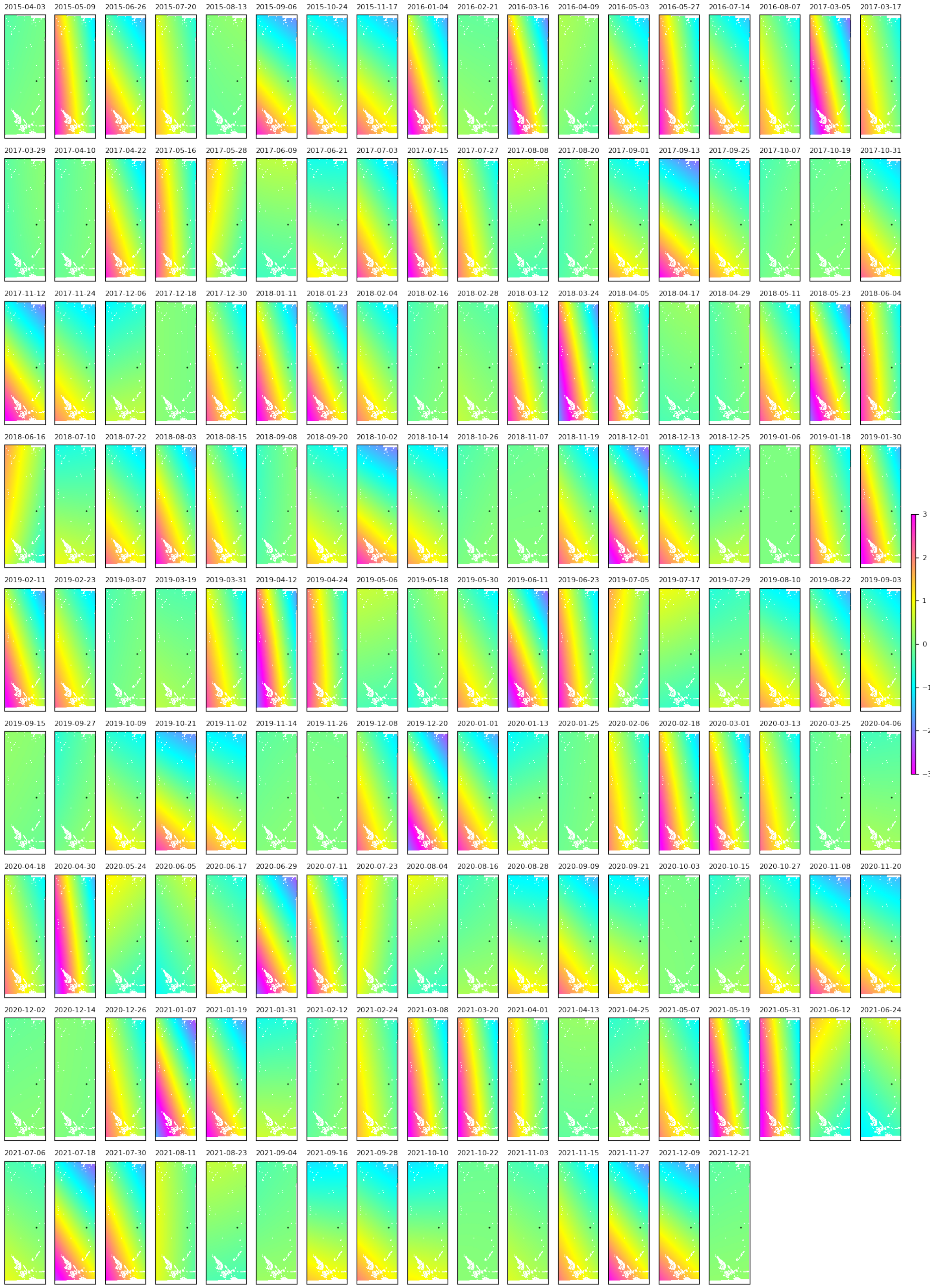

Figure S5. Similar to Fig. S4, but for the solid Earth tides phase time series. The data is rewrapped into [-3, 3) cm for display.

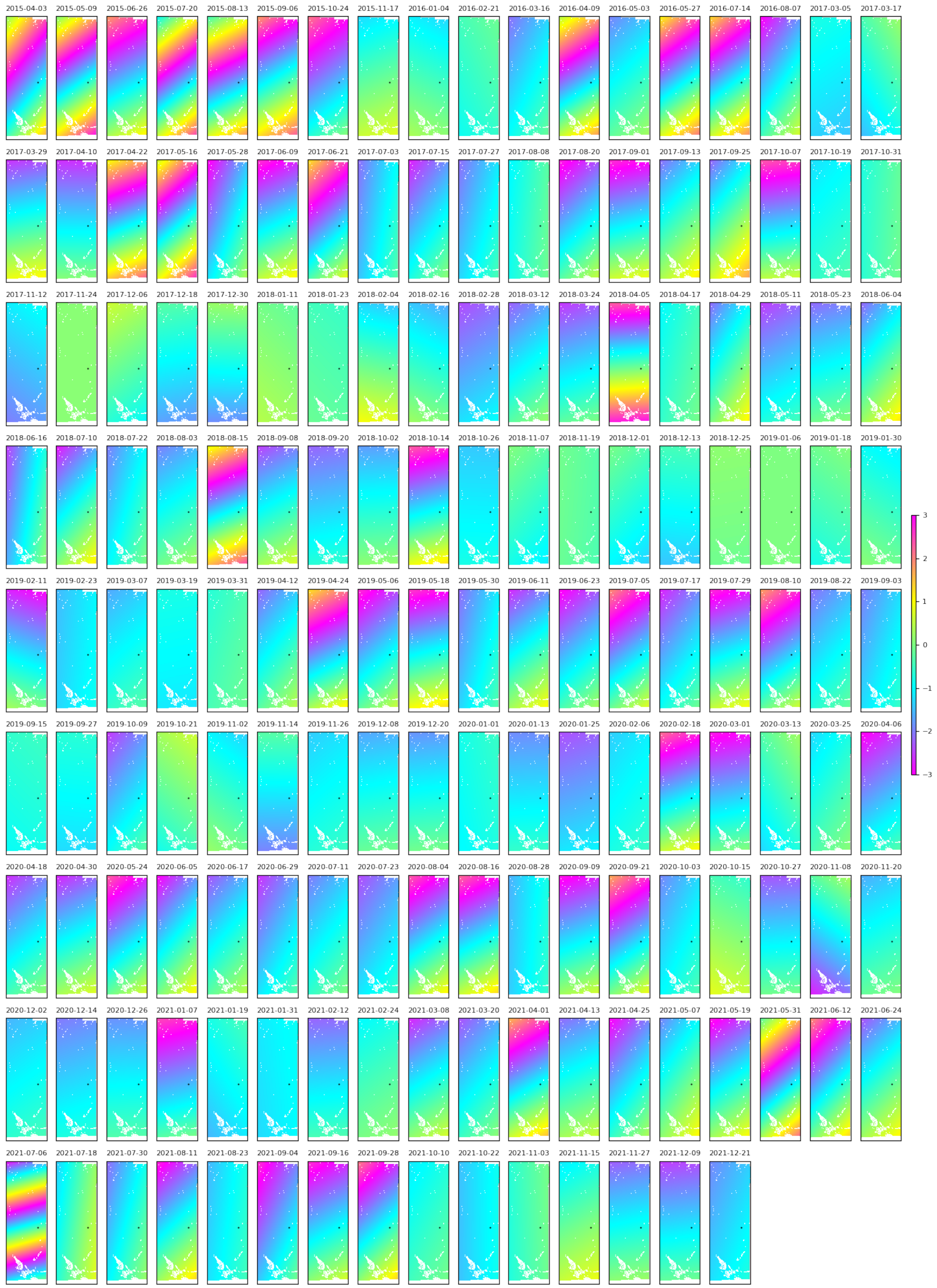

Figure S6. Similar to Fig. S4, but for the ionospheric delay phase time series using Madrigal TEC products. The data is rewrapped into [-3, 3) cm for display.

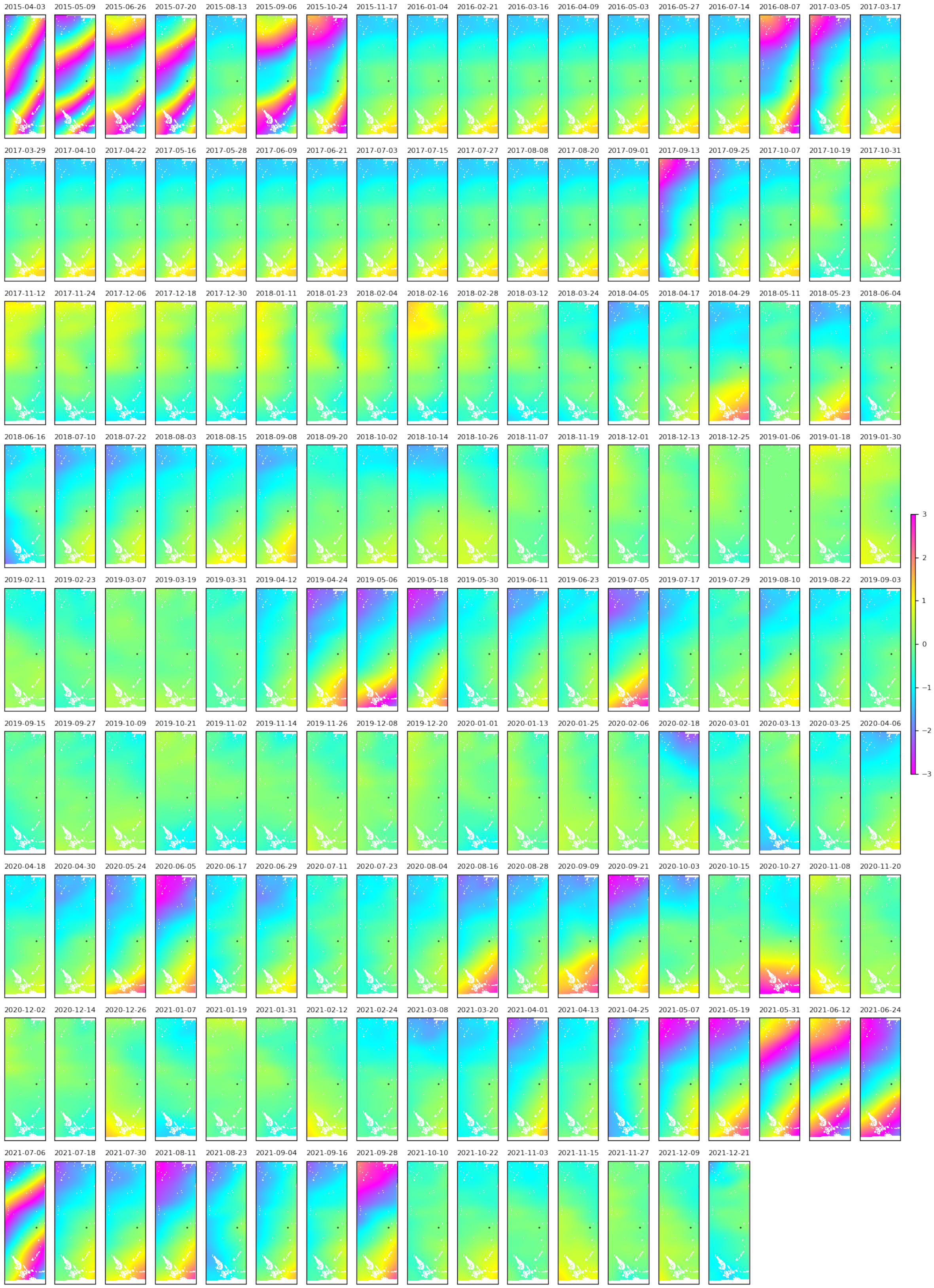

Figure S7. Similar to Fig. S4, but for the ionospheric delay phase time series using range split-spectrum method. The data is rewrapped into [-3, 3) cm for display.

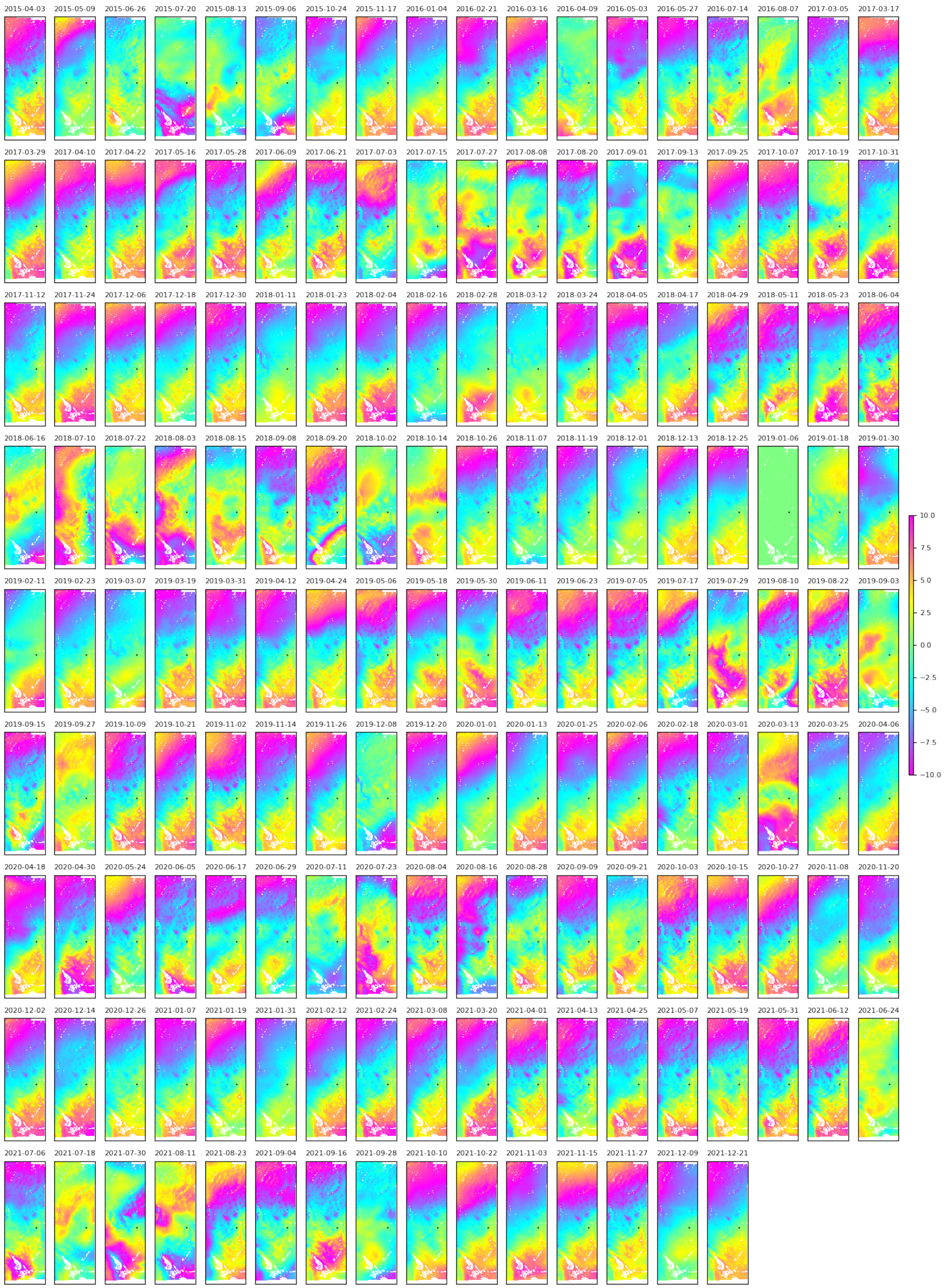

Figure S8. Similar to Fig. S4, but for the tropospheric delay phase time series using the ERA5 weather reanalysis data. The data is rewrapped into [-10, 10) cm for display.

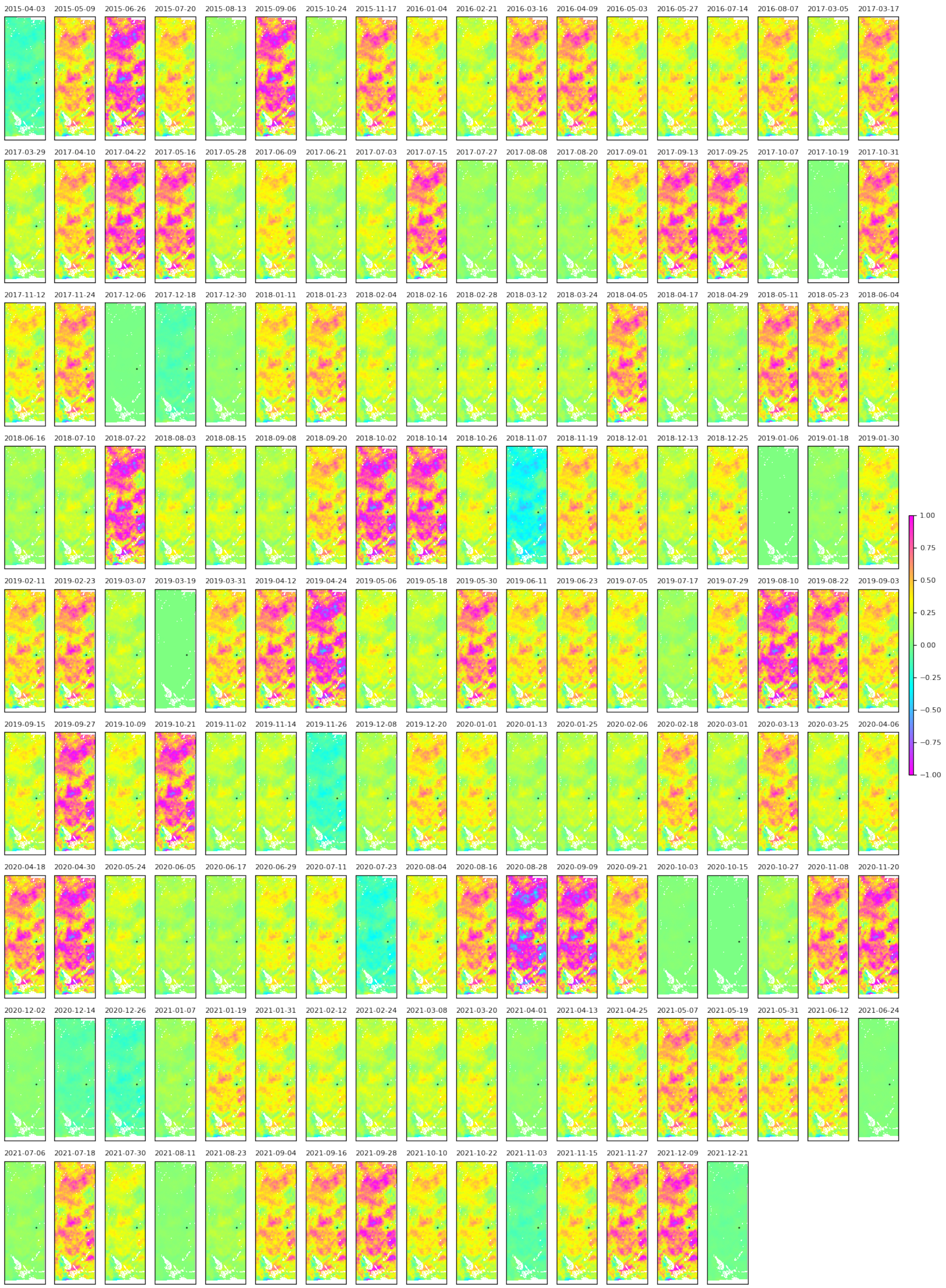

Figure S9. Similar to Fig. S4, but for the topographic residuals phase time series from DEM errors. The data is rewrapped into [-1, 1) cm for display.

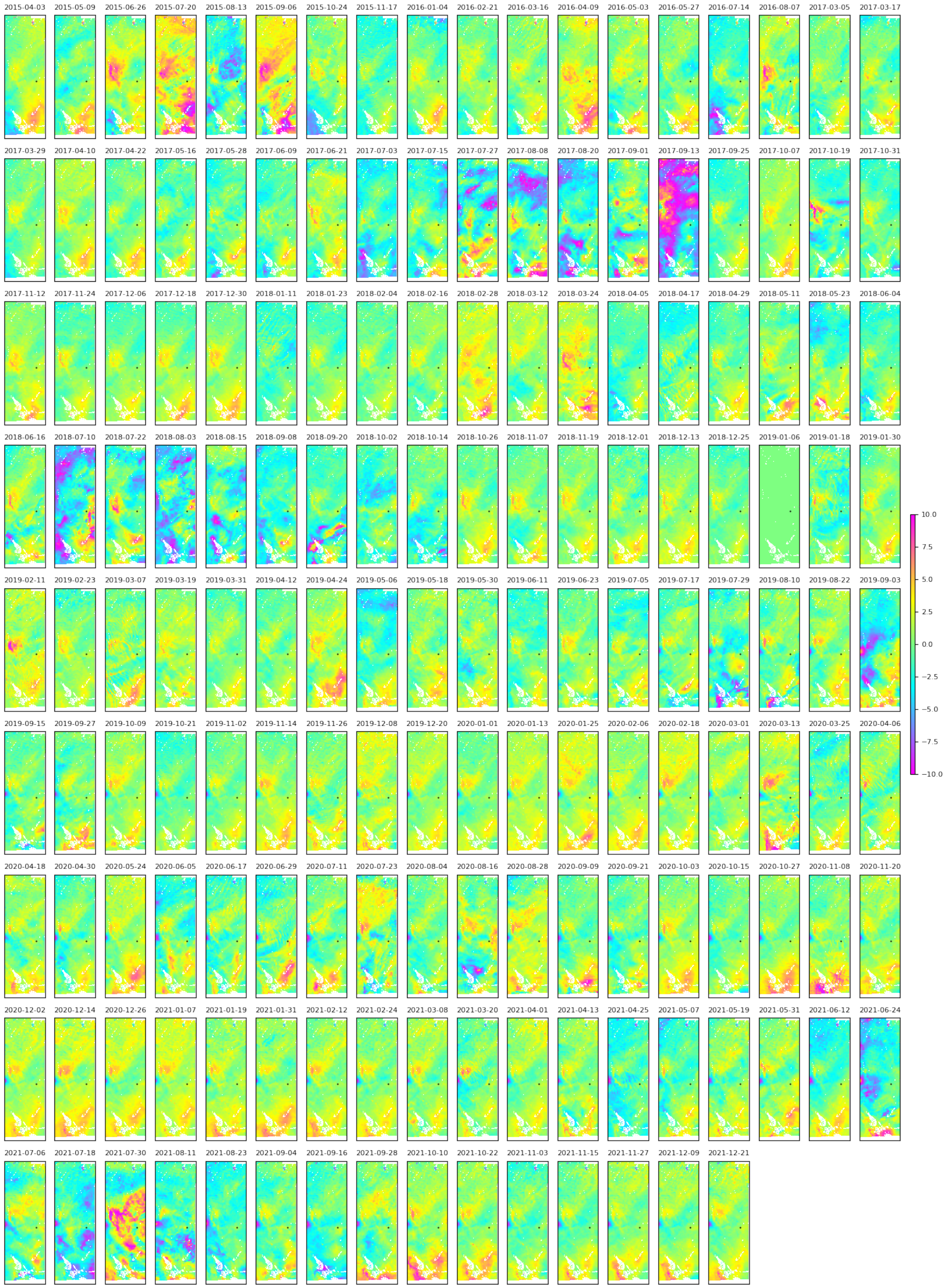

Figure S10. Similar to Fig. S4, but for the final displacement time series after correcting for solid Earth tides (Fig. S5), ionosphere (using Madrigal TEC products; Fig. S6), troposphere (Fig. S8), and topographic residuals (Fig. S9). The data is rewrapped into [-10, 10) cm for display.

S2. Sentinel-1 and ALOS-2 InSAR uncertainty due to orbit error

We estimated the orbital errors using the method from Fattahi & Amelung (2014) [3] using the actual satellite orbit parameters, as shown in table S1. The precision of Sentinel-1's precise orbits is better than 1 cm [4]. For ALOS-2, the cross-track orbit is very accurate with <8 cm in RMS in the worst case, while the along-track orbit RMS dominates the overall 3D orbit RMS, the latter is <25 cm [5]. Setting the azimuth correlation coefficient R=0.9 (conservative) [3], we obtained the potential contribution of the orbit error σ_r and σ_a on the InSAR secular velocity in the range and azimuth directions, respectively, as shown in table S1 below. For Sentinel-1, the impact of orbit error is less than 0.004 and 0.016 mm/year/100km in the range and azimuth directions, respectively; while for ALOS-2, it is less than 0.5 and 1.1 mm/year/100km in the range and azimuth directions, respectively. We estimated the contribution of orbital errors to the current estimated accuracy of our InSAR time series results, as shown in Table S2. Here, σ_{total_r} and σ_{total_a} denote the total orbital error in the range and azimuth directions, respectively, while $\sigma_{total} = \sqrt{\sigma_{total\_r}{}^2 + \sigma_{total\_a}{}^2}$ represents the total potential contribution of the orbital error.

Table S1 Orbit error calculation parameters and results

Sensor (Mode)	σ_{oh} [cm]	σ_{ov} [cm]	# of acquisition /year	Total time [year]	θ_0 [°]	$d\theta$ [°]	σ_r [mm/yr /100km]	σ_a [mm/yr /100km]
Sentinel-1 (IW)	1	1	25	9	29	7	0.004	0.016
ALOS-2 (ScanSAR)	25	8	5	7	24	7	0.30	0.66
ALOS-2 (StripMap)	25	8	10	4	4	7	0.5	1.1

Table S2 The contribution of orbital errors to the current estimated accuracy of our InSAR time series results

Track	Range coverage [100km]	Azimuth coverage [100km]	σ_{total_r} [mm/yr]	σ_{total_a} [mm/yr]	σ_{total} [mm/yr]
S1_D_USA	2.5	12	0.01	0.19	0.19
S1_D_Chile	2.5	8.5	0.01	0.14	0.14
S1_A_USA	2.5	7.5	0.01	0.12	0.12
S1_A_Chile	2.5	7.5	0.01	0.12	0.12
A2_D_USA	3.5	12	1.05	7.92	7.99
A2_D_Japan	0.5	1.5	0.25	0.28	0.38

S3. Displacement accuracy evaluation using independent GNSS displacements

We use the independent GNSS displacement time series from University of Nevada at Reno [6] as reference to evaluate the accuracy of the final InSAR deformation velocity, following the steps as below:

Step-1: Select GNSS stations based on the following two criteria: (1) The GNSS station should be within the spatial extent of the InSAR dataset. (2) The GNSS time series should overlap with the InSAR time series and have more than 50 observations within this overlapped time span with the InSAR dataset.

Step-2: Project the three dimensional GNSS displacement time series into the radar line-of-sight (LOS) direction. First, extract the GNSS displacement time series corresponding to the time span of the InSAR observations. Then, project the three-component (east, north, and vertical) displacements of GNSS into the LOS direction as follows:

$$d_{los} = \begin{bmatrix} d_e & d_n & d_u \end{bmatrix} \cdot \begin{bmatrix} (-1) \cdot \sin(\theta_{inc}) \cdot \sin(\theta_{az}) \\ \sin(\theta_{inc}) \cdot \cos(\theta_{az}) \\ \cos(\theta_{inc}) \end{bmatrix} \tag{S1}$$

where d_e, d_n, d_u denote the three-component (east, north, and vertical) displacements of GNSS, respectively; d_{los} represents the displacement of GNSS projected onto the LOS direction; θ_{inc} is the incidence angle from vertical, θ_{az} is the azimuth angle of the LOS vector from the ground to the SAR platform measured from the north with anti-clockwise direction as positive.

Step-3: Calculate the average velocities at each GNSS stations from GNSS and InSAR. (1) For both GNSS and InSAR, we choose a common spatial reference point at one GNSS stations for all datasets, whose ID are shown in Figs. 6-8 (except for the Sentinel-1 ascending track 149 in northern Chile, where we calculate the median velocity difference between the GNSS velocities and InSAR velocities at all GNSS stations and remove this difference from all GNSS velocities). (2) We estimate a linear velocity, and a Heaviside step function for each earthquake event where applicable (Figs. S11-S13), from each GNSS station and InSAR pixels. (3) For InSAR velocities, we interpolate the regularly gridded InSAR data at each GNSS stations using a linear interpolator, to account for the potential location difference between the GNSS station and InSAR pixel center [7].

Step-4: Calculate the root mean square error (RMSE) and the coefficient of determination R^2 between GNSS and InSAR velocities on all stations for each InSAR dataset, following equation (7)-(8).

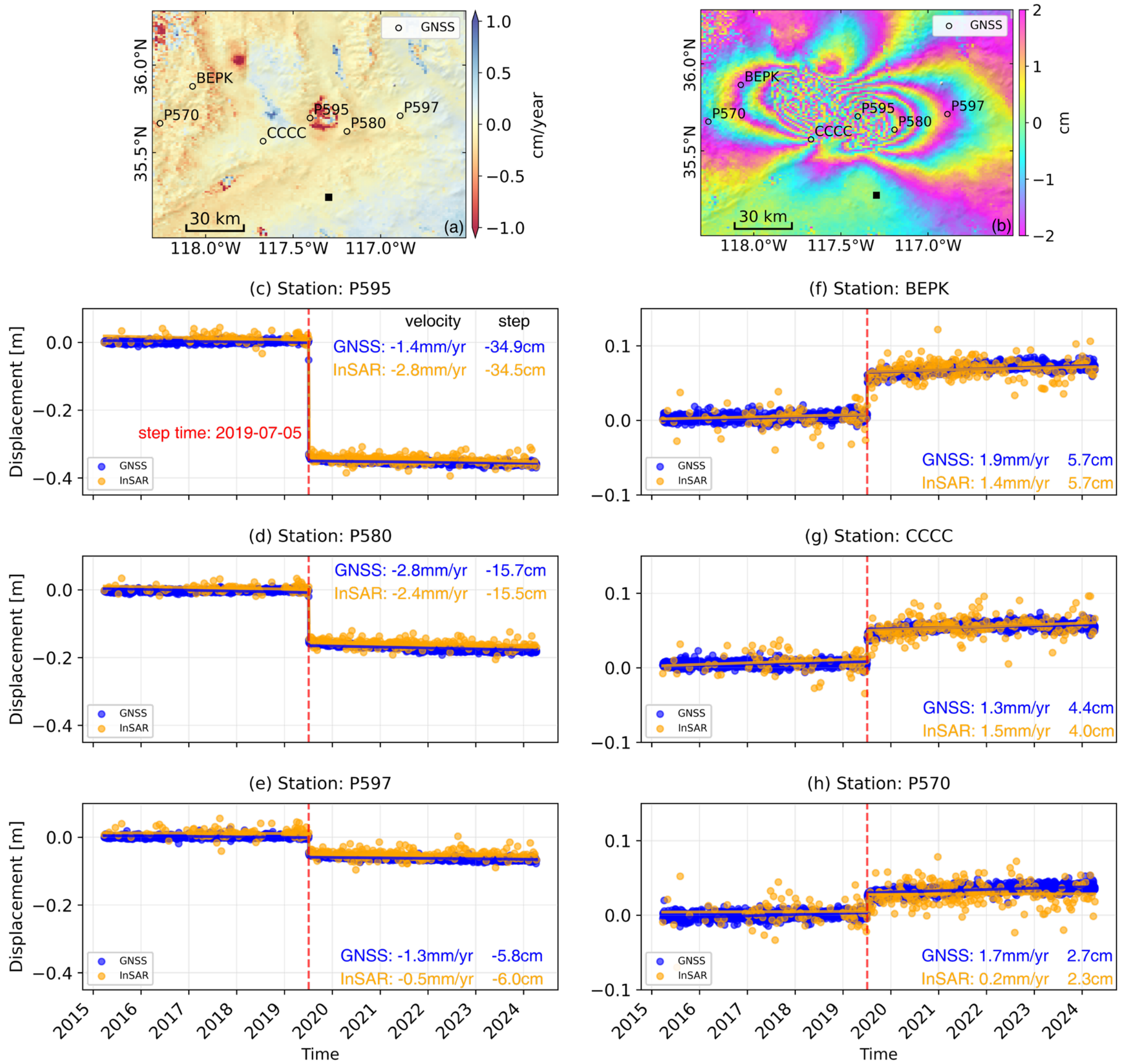

Figure S11. Comparison of InSAR and GNSS time series for Sentinel-1 ascending track 064 in western USA account for the impact of the 2019 Ridgecrest earthquakes on 2019-07-04 and 2019-07-05 [8]. (a)-(b) Estimated linear velocity and Heaviside step function at 2019-07-05. The black square denotes the reference point at GNSS station P592. The estimated step function is re-wrapped into [-2, 2) cm for display. (c)-(h) InSAR and GNSS time series for all GNSS stations within ~70 km from the earthquake epicenter.

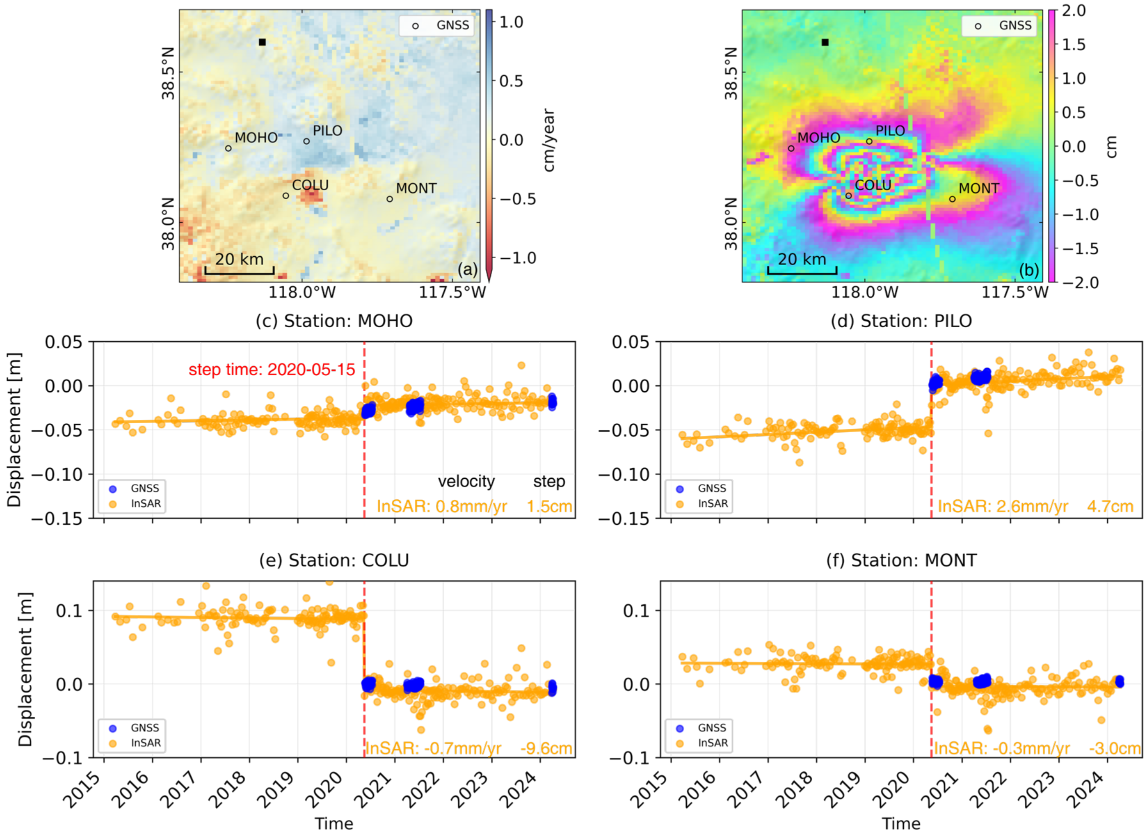

Figure S12. Comparison of InSAR and GNSS time series for Sentinel-1 ascending track 064 in western USA account for the impact of the 2020 Monte Cristo Range earthquake on 2020-05-15 [9]. (a)-(b) Estimated linear velocity and Heaviside step function at 2020-05-15. The black square denotes the reference point at GNSS station CALA. The estimated step function is re-wrapped into [-2, 2) cm for display. (c)-(f) InSAR and GNSS time series for all GNSS stations within ~40 km from the earthquake epicenter. According to the GNSS screening criteria described in section S3, the GNSS time series does not have more than 50 observations within the span with the InSAR dataset., so no GNSS comparison is performed.

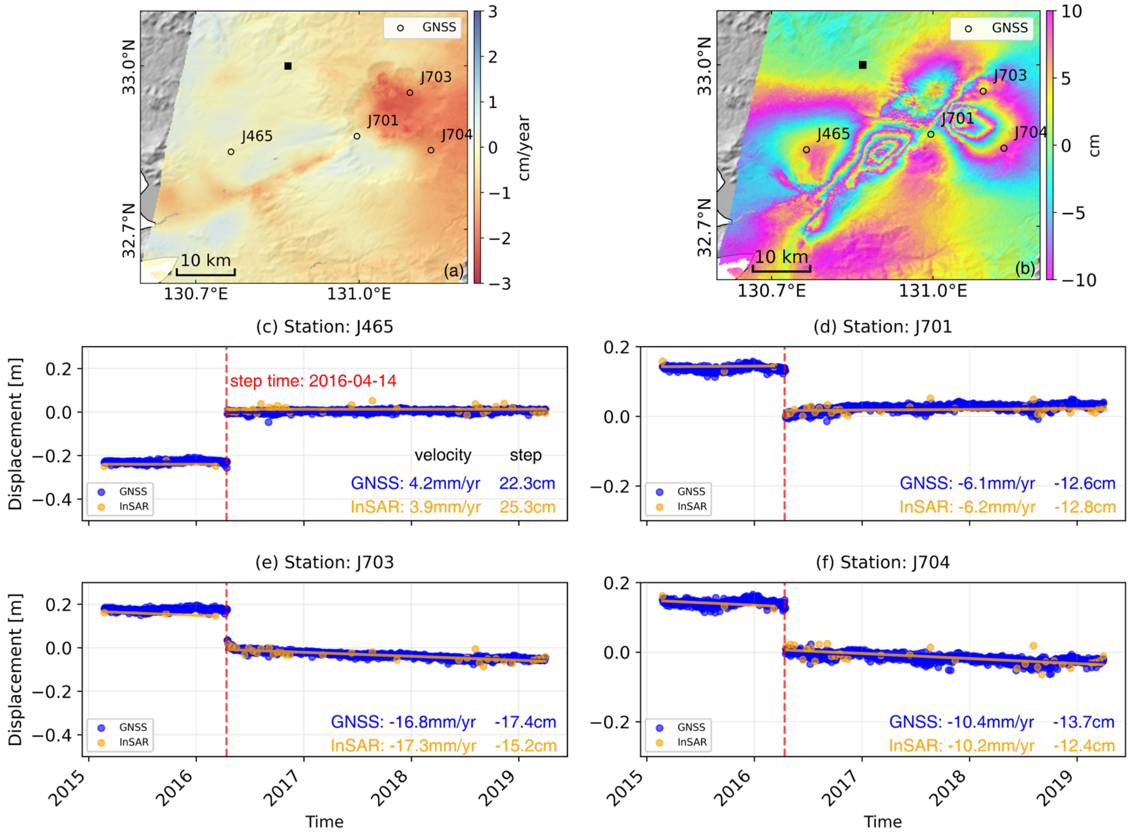

Figure S13. Comparison of InSAR and GNSS time series for Sentinel-1 ascending track 064 in western USA account for the impact of the 2016 Kumamoto earthquake on 2016-04-14 [10]. (a)-(b) Estimated linear velocity and Heaviside step function at 2016-04-14. The black square denotes the reference point at GNSS station G070. The estimated step function is re-wrapped into [-10, 10) cm for display. (c)-(f) InSAR and GNSS time series for all GNSS stations within ~30 km from the earthquake epicenter.

Supplemental references

[1] P. S. Agram, and M. Simons, "A noise model for InSAR time series," *J. Geophys. Res.*: Solid Earth, vol. 120, no. 4, pp. 2752-2771, 2015. DOI: 10.1002/2014JB011271.

[2] A. Pepe, and R. Lanari, "On the Extension of the Minimum Cost Flow Algorithm for Phase Unwrapping of Multitemporal Differential SAR Interferograms," *IEEE Trans. Geosci. Remote Sens.*, vol. 44, no. 9, pp. 2374-2383, 2006. DOI: 10.1109/TGRS.2006.873207.

[3] H. Fattahi, and F. Amelung, "InSAR uncertainty due to orbital errors," *Geophys. J. Int.*, vol. 199, no. 1, pp. 549-560, Aug. 2014. DOI: 10.1093/gji/ggu276.

[4] M. Fernández, H. Peter, D. Arnold, et al., "Copernicus Sentinel–1 POD reprocessing campaign," Adv. Space Res., vol. 70, no. 2, pp. 249-267, 2022. DOI: 10.1016/j.asr.2022.04.036.

[5] K. Akiyama, H. Itoh, H. Masuda, et al., "Operational Validation of Precise Orbit Determination for ALOS-2," in SpaceOps 2016 Conference. 2016. DOI: 10.2514/6.2016-2521.

[6] G. Blewitt, W. Hammond, and C. Kreemer, "Harnessing the GPS Data Explosion for Interdisciplinary Science," *Eos*, vol. 99, no. 2, e2020943118, Sep. 2018. DOI: 10.1029/2018eo104623.

[7] Z. Yunjun, H. Fattahi, and F. Amelung, "Small baseline InSAR time series analysis: Unwrapping error correction and noise reduction," *Comput. Geosci.*, vol. 133, p. 104331, 2019. DOI: 10.1016/j.cageo.2019.104331.

[8] X. Xu, D. T. Sandwell, L. A. Ward, et al., "Surface deformation associated with fractures near the 2019 Ridgecrest earthquake sequence," *Science*, vol. 370, no. 6516, pp. 605–608, 2020. DOI: 10.1126/science.abd1690.

[9] T. Sadeghi Chorsi, J. Braunmiller, F. Deng, and T. H. Dixon, "Afterslip From the 2020 M 6.5 Monte Cristo Range, Nevada Earthquake," *Geophys. Res. Lett.*, vol. 49, no. 17, e2022GL099952, 2022. DOI: 10.1029/2022GL099952.

[10] H. Yue, Z. E. Ross, C. Liang, et al., "The 2016 Kumamoto Mw = 7.0 Earthquake: A Significant Event in a Fault-Volcano System," *J. Geophys. Res. Solid Earth*, vol. 122, no. 11, pp. 9166–9183, 2017. DOI: https://doi.org/10.1002/2017JB014525.